

Article

Lightweight Robotic Joint with Thermally Activated Paraffin Actuator in the Deep Sea

Dayong Ning¹, Xiaokang He², Jiaoyi Hou^{1,*}, Gangda Liang² and Kang Zhang¹ 

¹ National Center for International Research of Subsea Engineering Technology and Equipment, Dalian Maritime University, Dalian 116026, China; ningdayongning@vip.163.com (D.N.); zhangkang@dmlu.edu.cn (K.Z.)

² Department of Marine and Ocean Engineering, Dalian Maritime University, Dalian 116026, China; hxk233@foxmail.com (X.H.); lianggangda@dmlu.edu.cn (G.L.)

* Correspondence: houjiaoyi@vip.163.com

Abstract: The abundance of resources in the deep sea continues to inspire mankind's desire for exploration. However, the extreme environments pose a huge challenge for designing deep-sea mechanical devices that are primarily driven by hydraulic and electric motor technology. Researchers are beginning to explore more flexible and innovative drive methods suitable for the deep-sea environment. This paper presents a simple joint mechanism based on a paraffin phase change thermal expansion drive. Its unique design combines a flexible cell with an open structure that allows it to adapt to different pressures at different water depths. Paraffin is enclosed in multiple sets of smaller paraffin cells, which act as thermal expansion material for generating hydraulic pressure. The software comsol was used to perform a finite element analysis of the phase change process in paraffin. By fabricating the mechanical structure, the displacement generated by the thermal expansion is amplified and converted, thus enabling a bi-directional rotational displacement output from the joint while reducing the complexity of the structure. The joints in this paper provide a reliable reference for the design of small deep-sea robot drive systems.

Keywords: deep sea; actuator; paraffin; mechanical joints; soft actuator



Citation: Ning, D.; He, X.; Hou, J.; Liang, G.; Zhang, K. Lightweight Robotic Joint with Thermally Activated Paraffin Actuator in the Deep Sea. *J. Mar. Sci. Eng.* **2023**, *11*, 2253. <https://doi.org/10.3390/jmse11122253>

Academic Editor: Weicheng Cui

Received: 7 November 2023

Revised: 25 November 2023

Accepted: 27 November 2023

Published: 29 November 2023



Copyright: © 2023 by the authors. Licensee MDPI, Basel, Switzerland. This article is an open access article distributed under the terms and conditions of the Creative Commons Attribution (CC BY) license (<https://creativecommons.org/licenses/by/4.0/>).

1. Introduction

The ocean covers more than 97% of the Earth's surface and possesses abundant resources. Within the realm of marine exploration, the deep sea (defined as areas with depths exceeding 200 m) accounts for over 95% of the global ocean volume, making it the largest and least developed marine domain on our planet [1]. The environmental complexity and biodiversity of the deep-sea environment hold significant importance for humans and the Earth's ecological systems [2,3]. Nevertheless, the deep-sea environment exhibits distinct and extreme characteristics, such as low water temperatures and high pressures [4], which pose immense challenges to the design and application of underwater operational equipment and actuators.

Taking conventional deep-sea robots, such as AUVs (autonomous underwater vehicles) and ROVs (remotely operated vehicles), as examples, their drive system typically employ rigid components and are primarily driven by hydraulic and electric mechanisms [5]. Researchers often need to design complex sealing mechanisms and heavy pressure-resistant housings to adapt the actuator to high environmental pressure, which makes it difficult to achieve lightweight designs and results in high manufacturing and maintenance costs [6–8].

The limitations of traditional drive systems have become evident. Recent years, research on bio-inspired soft underwater machines has also been developing rapidly. Pawandeeep Singh Matharu et al. designed a 3D printed biomimetic soft jellyfish robot with flexible TPU material, driven by NiTi Flexinol spring actuators [9]. This robot has a simpler

structure and better vertical swimming displacement performance than other jellyfish-inspired robots. Li et al. designed a deep-sea snailfish-inspired soft-bodied robot [10]. The robot is powered by DE artificial muscles and has a body made of a silicone matrix with electronics embedded inside for pressure resistance. Li et al. proposed a robotic injection drive method for high-pressure environments using high-frequency vibration of piezoelectric vibrators [11]. The proposed robot exhibits the merits of miniature size, high agility, and high mobility. These mechanisms have diverse driving principles, strong pressure resistance, simple structure, and minimal environmental impact during operation, to some extent compensating for the limitations of traditional drive systems [12]. However, there are also issues such as high driving voltage, material instability, and low output force.

In recent years, with the deepening of research, paraffin phase change materials (PCM) have demonstrated tremendous development potential in various fields. Paraffin is a typical solid–liquid phase change material with high bulk modulus, stable chemical properties, low cost, and a phase change process that can generate about 10–20% thermal expansion [13]. Ogden et al. compared paraffin with other new materials and found that paraffin has the highest energy density [14]. Based on these characteristics, researchers have explored the potential applications of paraffin in fields such as actuators [15], micro-pumps [16], and micro-valves [17]. In the application of deep-sea devices, Hou et al. designed a flexible biomimetic bony fish bladder using the volume and density difference between the two phases of paraffin before and after phase change [18]. The aim was to achieve buoyancy adjustment in small deep-sea devices. By inputting heat through internal heating wires, the paraffin material undergoes phase change, thereby changing the overall density to achieve buoyancy regulation. NING et al. designed a deep-sea micro-paraffin phase change actuator [19], which is enclosed by a flexible shell to achieve pressure adaptation. Internal heating devices are used to heat the paraffin to induce phase change and generate a volume increment. A radial limiting device is added to the outer periphery of the flexible shell to obtain axial displacement. Testing showed that this device was able to stably output significant linear displacement under a static water pressure of 110 MPa.

However, there is currently limited research on deep-sea paraffin phase-change material (PCM) actuators. Existing paraffin PCM actuators have a single output form. Therefore, it is essential to investigate high-efficiency, diverse-output, and practically reliable PCM-driven actuation mechanisms to cater to the diverse needs of deep-sea exploration. As a result, this paper presents the design of a small-scale joint structure based on paraffin phase-change actuation, capable of bidirectional rotation, for application in deep-sea small robotic systems. The remaining sections of this paper initially describe the model of a linear actuator based on paraffin PCM. The paraffin phase-change process is numerically analyzed, and a mathematical model for the elongation of a corrugated tube actuation unit under no-load conditions is established. Subsequently, building upon the aforementioned actuator, a bidirectional rotational joint mechanism is designed, and performance testing experiments are conducted. This article concludes by summarizing its findings and outlining potential areas for future research.

2. Materials and Methods

Section 2.1 describes the design concept and analysis process of the bellows drive unit based on the paraffin phase change drive, and Section 2.2 describes the process of designing, fabricating and analyzing the drive mechanism of the mechanical joints based on the drive unit in the previous section, as shown in Figure 1.

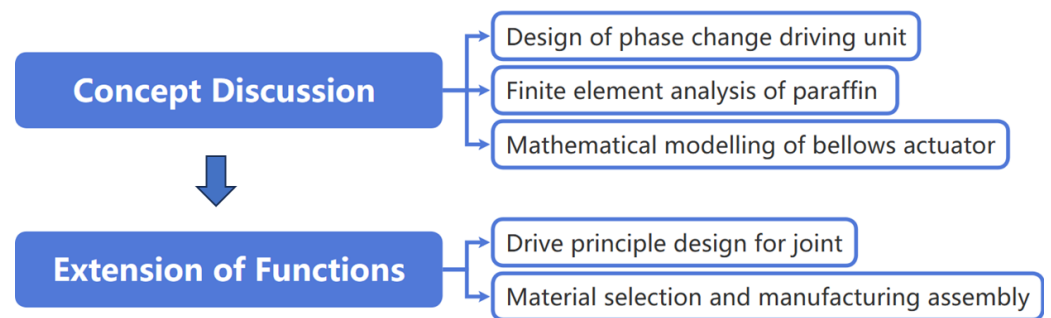


Figure 1. Schematic block diagram of this section.

2.1. Design and Analysis of Paraffin Phase Change Flexible Actuator

2.1.1. Analysis of the Actuator Principle

Utilizing the thermal expansion characteristics of paraffin, a linear actuator driven by paraffin PCM has been designed, as shown in Figure 2. The paraffin PCM is encapsulated in a flexible skin to form independent units, which was finally placed inside a rigid shell. The required heat for paraffin phase change is provided by an electric heating device. The flexible casing effectively restricts the flow of liquid phase paraffin, allowing the paraffin units to return to their original positions after each phase change cooling, ensuring the repeatability of the actuator for multiple works. The rigid shell is connected to the flexible bellows, and the remaining parts in bellows and rigid shell are filled with a liquid medium. The volume increment generated during the phase change is transmitted to the flexible bellows through the liquid medium, causing it to undergo deformation and perform external work. In high-pressure environments, the liquid will inevitably experience certain compression. By employing an open design for the actuator, the high elastic modulus of the flexible material generates deformations Figure 2a that compensate for the volume compression, thereby achieving pressure self-adaptation. The paper selected silicone bellows as the flexible actuating mechanism for the actuator Figure 2b. The unique corrugated structure of the silicone bellows is favorable for generating larger unidirectional displacement.

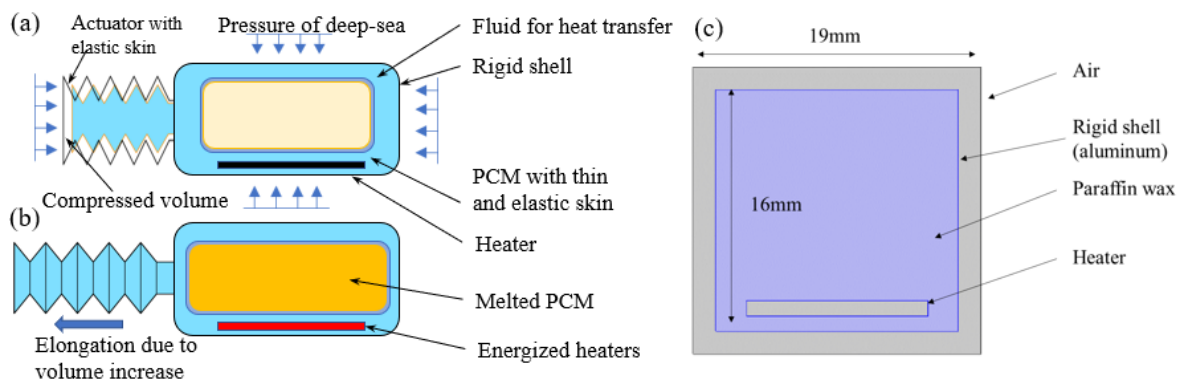


Figure 2. (a) Brief structure of the driver; (b) brief structure of the driver; (c) boundary conditions of the physical model for paraffin phase change cavity. The Z dimension is 150 mm.

2.1.2. Establishment and Numerical Analysis of PCM Heat Transfer Model

This paper intends to establish a mathematical heat transfer model for paraffin phase change based on the “enthalpy–porosity model” in comsol and solve it [20]. A physical model of the chamber filled with paraffin PCM is constructed, with a strip-shaped electric heating device placed inside. To simplify the calculations, a cross-section of the chamber as shown in Figure 2c is studied and analyzed. The overall dimensions of the chamber are 19 mm × 19 mm, with a wall thickness of 1.5 mm. The shell is surrounded by air, and the interior is filled with paraffin phase change material, with the electric heating device

placed beneath the shell. The enthalpy–porosity model treats the coexistence region of solid–liquid during the phase change (slurry zone) as a porous medium, and the liquid fraction is characterized by the porosity, which varies from 0 to 1 during the PCM melting process. This study has selected 58# paraffin as the phase change material, and its physical properties are shown in Table 1.

Table 1. Thermophysical properties of 58# paraffin.

Properties	Dimensions	Value
Density of solid paraffin (ρ_{solid})	Kg/m ³	900
Density of liquid paraffin (ρ_{liquid})	Kg/m ³	773
Thermal conductivity of Solid paraffin (k_{solid})	W/(m·K)	0.28
Thermal conductivity of Liquid paraffin (k_{liquid})	W/(m·K)	0.14
Constant pressure heat capacity (c_p)	J/(kg·K)	2200
Dynamic viscosity of liquid paraffin (μ)	Pa·s	0.003
Coefficient of cubical expansion (α)	1/K	0.0015
Solid phase temperature line (T_S)	K	331.15
Solid phase temperature line (T_L)	K	337.15
Latent heat (L)	kJ/kg	250.6

Comsol was used to simulate the phase change of paraffin. The heating device was set to input a constant power of 48 W to the PCM. The temperature field and phase field of the chamber section within 50 s are shown in Figure 3.

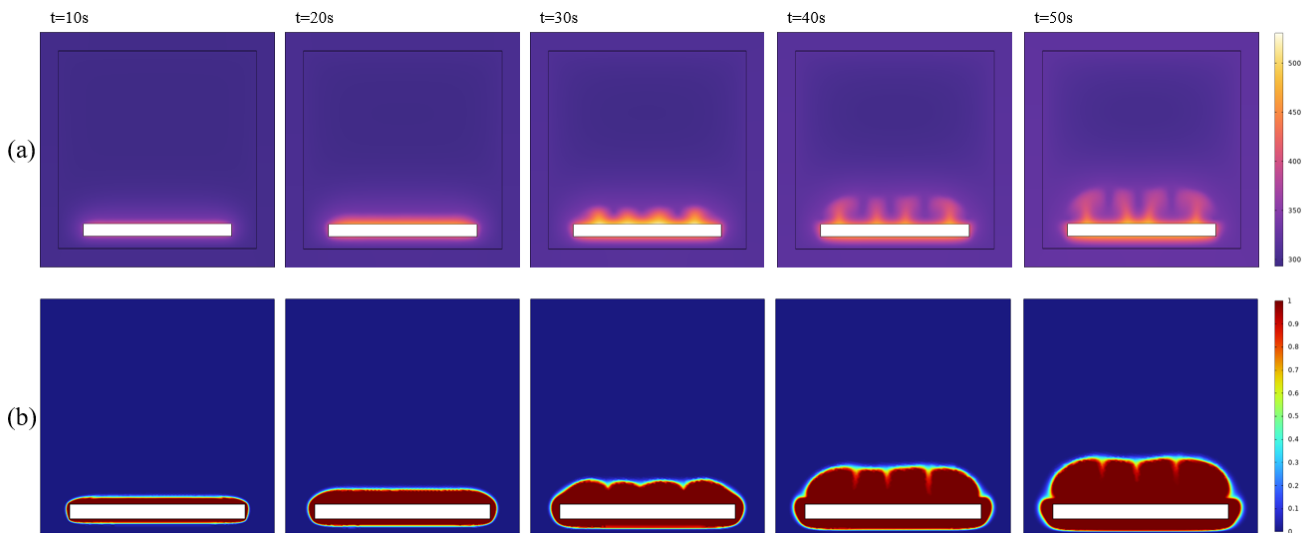


Figure 3. (a) Snapshot of the temperature field distribution of the entire actuator within 0–50 s; (b) snapshot of the phase field distribution of the paraffin unit within 0–50 s.

Combining temperature field and phase field, it can be observed that as the volume fraction of liquid phase paraffin increases, the heat convection phenomenon caused by density differences becomes more pronounced. This phenomenon promotes the melting of paraffin and leads to significant differences in the melting rate between the upper and lower sides of the heating device. Additionally, in Figure 3a, it can be noticed that due to the heating device being located close to the bottom wall of the shell, the liquid phase paraffin quickly spreads and contacts the inner wall of the shell, resulting in the faster temperature increase of the shell.

Assuming that the phase distribution of paraffin units during the phase transition process within the cavity remains the same across any cross-section, this paper approxi-

mates the paraffin phase transition in the two-dimensional cross-section as equivalent to the paraffin melting process in the three-dimensional cavity. The liquid phase fraction can characterize the proportion of liquid phase within the paraffin material, representing the degree of paraffin material melting:

$$\beta = \begin{cases} 0 & (T < T_s) \\ \frac{(T-T_s)}{(T_L-T_s)} & (T_s < T < T_L), \\ 1 & (T > T_L) \end{cases} \quad (1)$$

where T_s is the solid phase temperature line of the PCM, representing the phase change starting temperature, and T_L is the liquid phase temperature line of the PCM, representing the phase change termination temperature. When β is equal to 0, the PCM is in the solid state; when β is equal to 1, the PCM is in the liquid state; and when the value of β is between 0 and 1, the PCM is in a mushy state.

Additionally, since the melting of paraffin is directly related to its volume expansion, in the subsequent modeling work of this paper, the liquid phase fraction is considered to be a relevant parameter for calculating the thermal expansion of phase-transitioning materials, as shown in the following equation.

Additionally, since the melting of paraffin is directly related to its volume expansion, in the subsequent modeling work of this paper, the liquid phase fraction is considered to be a relevant parameter for calculating the thermal expansion of phase-transitioning materials, as shown in the equation:

$$\Delta_v = V_f \cdot \beta \cdot f \quad (2)$$

where Δ_v represents the volume increment generated by the entire paraffin material, V_f represents the total volume of the paraffin, β represents the liquid phase fraction of the paraffin, and f represents the thermal expansion rate of the standard-grade paraffin.

2.1.3. Mathematical Model for Expansion Based on Bellows Actuator

The geometry of the bellows actuator is shown in Figure 4a. Assuming that the diameter of the wave trough of bellows remains constant during the process of elongation affecting the external displacement and neglecting the wall thickness of the bellows and wall surface expansion during the dilation process, this paper established a mathematical relationship between the incremental volume of the corrugated tube chamber and the elongation rate.

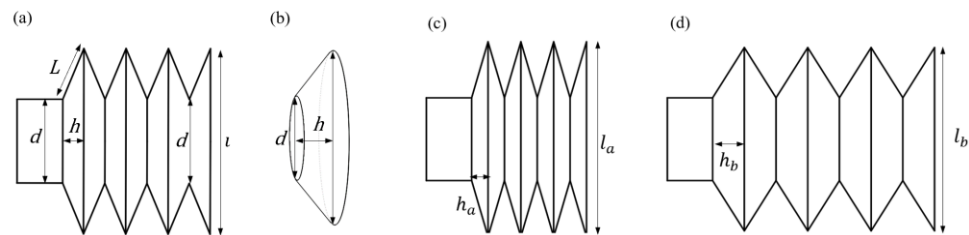


Figure 4. (a) Simplified geometric structure of the bellows; (b) individual conical dimensions of the bellows; (c) compressed bellows; (d) extended bellows.

The volume increment during the elongation process is considered the sum of incremental volumes of multiple frustum cones (Figure 4b).

The relationship between the volume increment Δ_{v1} and the height of the frustum cone h is obtained using the formula for the volume of a frustum cone:

$$\Delta_{v1} = \frac{1}{3} \cdot n \cdot \pi \cdot h \cdot \left[\left(\frac{d}{2} \right)^2 + \left(\frac{d + 2\sqrt{L^2 - h^2}}{2} \right)^2 + \frac{d}{2} \cdot \frac{d + 2\sqrt{L^2 - h^2}}{2} \right] - V_0 \quad (3)$$

where Δ_{v1} represents the increase in internal volume due to the elongation of the bellows, n represents the number of round tables contained in the bellows, h represents the height of a single round table unit, d represents the diameter of the trough of the bellows, L represents the waist length of the trapezoid of the circular table section, and V_0 represents the internal volume of the initial length of the bellows.

In the design of this actuator, the cavity of the paraffin phase change is directly connected to the bellows, which means that the volume increment of the paraffin phase change directly leads to the expansion of the internal volume of the bellows. The volume increment Δ_{v1} of the bellows chamber is equal to the phase change volume increment Δ_v :

$$\Delta_{v1} = \Delta_v \tag{4}$$

Therefore, in order to obtain the relationship between the key parameter “liquid phase rate” and the elongation of the bellows during the phase change process of paraffin, we simplify the equation to obtain the following relationship:

$$\beta = \frac{\frac{1}{3} \cdot n \cdot \pi \cdot h \cdot \left[\left(\frac{d}{2}\right)^2 + \left(\frac{d+2\sqrt{L^2-h^2}}{2}\right)^2 + \frac{d}{2} \cdot \frac{d+2\sqrt{L^2-h^2}}{2} \right] - V_0}{V_f \cdot f} \tag{5}$$

The mathematical model expressed in the above equation has two variables: h and β . From the study in Section 2.1.1, β can be used as input and h is the output of the bellows actuator based on the simulation data. Equation (5) establishes the relationship between the parameters of paraffin phase transition and actuator elongation in a bellows actuator.

But as h is the elongation of a single circular table, the elongation of the entire bellows actuator needs to be accumulated by the following equation:

$$H = n \cdot h \tag{6}$$

where H represents the total elongation of the bellows.

2.2. Structure and Analysis of the Joint

2.2.1. Structural Design, Manufacture, and Assembly

Based on the concept of modular design, this paper expanded the structure and functionality of the previously mentioned phase transition driving device, as shown in Figure 2a. A rotation joint mechanism with a simple structure and compact dimensions was designed. This mechanism can achieve a rotational displacement of 120° and is capable of operating in the deep sea. The overall structure is depicted in Figure 5e. Table 2 describes the materials and processing methods involved for the fabrication and assembly steps.

Table 2. The materials and fabrication of the joint.

Module	Part Name	Materials	Fabrication
PCM storage unit	PCM units	paraffin+ silicone rubber	glue seal
PCM storage unit	heaters	PTC ceramic heaters	-
PCM storage unit	liquid medium	C2H4(OH)2	-
transmission unit	gears and racks	brass	-
transmission unit	supporting shell	resinous	3D printing
transmission unit	gear shaft	stainless steels	turning
transmission unit	bellows	rubber	-
valve unit	valve body	aluminum alloy	NC machining
valve unit	membrane	silicone rubber	demolding
reflow unit	flexible chamber	silicone rubber	demolding

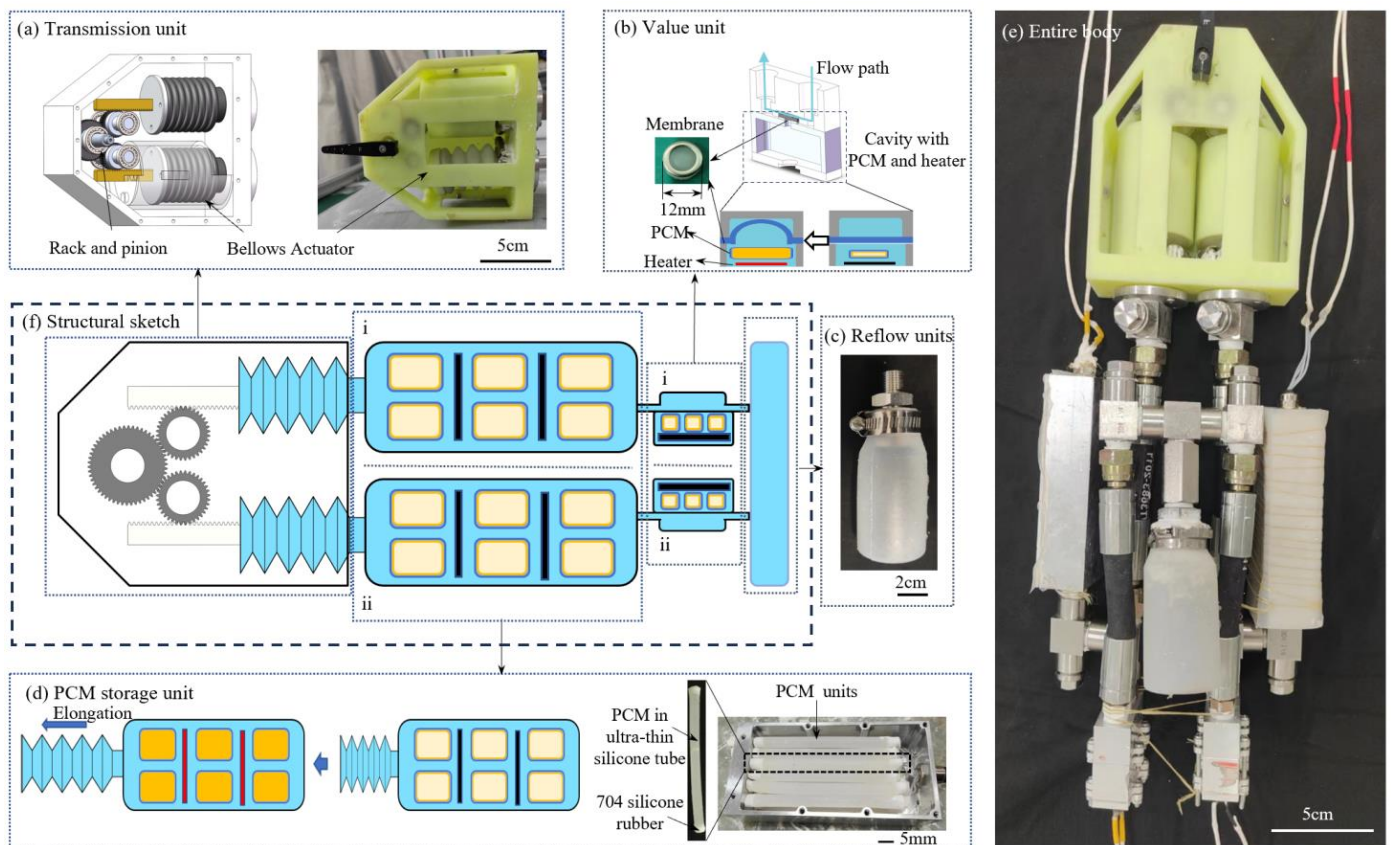


Figure 5. (a) Transmission unit—employing gears and racks to convert the linear output of the corrugated tube into rotational motion; (b) valve unit—utilizing paraffin phase change to pressurize a thin membrane in the flow path, causing it to deflect and block the flow path; (c) reflow unit—its unique flexible outer shell enables unrestricted expansion or contraction to accommodate reflux fluid while balancing internal and external pressures; (d) PCM storage unit—internally containing paraffin, heat-transfer fluid, and electric heating devices encapsulated by ultra-thin silicone tubes. The volume increment of PCM conducted into the corrugated tube actuator cavity through the heat-conductive fluid; (e) manufacturing and assembly diagram of the paraffin PCM-driven phase change joint; (f) structure of the paraffin PCM-driven joint.

Figure 5d shows the PCM storage unit, where a group of paraffin units is placed inside a rigid shell. The required energy for the phase change is supplied by the electric heating device. The paraffin unit is a tubular paraffin encapsulated by an ultra-thin silicone tube (diameter 6 mm, thickness 0.1 mm).

Figure 5a shows the transmission unit, which is responsible for converting the linear displacement obtained from the bellows into rotational displacement through a gear mechanism. This module consists of a gear reduction transmission mechanism, rack, bellows, and a supporting shell. The joint is designed with two symmetrical bellows mechanisms connected to the two PCM storage units. The rack fixed on the bellows is symmetrically arranged on both sides of the gear reduction mechanism. This symmetrical arrangement can convert the linear displacement generated by two bellows into opposite rotational displacement, effectively amplifying the working range and response speed compared to the output of a single bellows. The data of paraffin expansion rate and bellows used in this study are presented in Table 3.

Table 3. The geometric data for bellows and the thermal expansion rate of the 58# paraffin.

Properties	Dimensions	Value
total volume of the paraffin (V_f)	cm ³	45.78
thermal expansion rate (f)	-	0.17
number of round tables (n)	-	7
diameter of the trough of the bellows (d)	cm	2.27
waist length of the trapezoid of the circular table (L)	cm	0.77
Initial height of a single round table (h_0)	cm	0.17

Figure 5c shows the reflow unit, which serves the function of storing the backflow liquid generated when one end of the bellows is compressed. The material used for this chamber is silicone. Due to the coupled action of the two bellows assembly positions, the volume increase and elongation of one bellows inevitably correspond to the volume decrease and contraction of the other bellows, causing the liquid to flow back into the flexible chamber. Moreover, under the natural state, this chamber is connected to the bellows and PCM storage units. In high-pressure environments, the volume compression caused by the liquid and the presence of air bubbles during the manufacturing process are compensated by the deformation of the flexible outer skin, thus preventing the rigid structure from being crushed.

Figure 5b shows the valve unit, which functions to control the on/off state of the flow path, determining the start and stop of the joint. It mainly consists of a metal body, silicone membrane, paraffin PCM, heating device, and thermal fluid. The principle of operation is similar to the paraffin PCM actuator. When the PCM material undergoes volume expansion, it increases the volume of the liquid inside the chamber, causing the silicone membrane to bulge and block the flow path. By changing the connection state between the PCM storage unit and the reflow unit, the control of joint start and stop actions can be achieved.

2.2.2. Working Mechanism

The working mechanism of this joint is as follows:

1. Heat the flow valve i chamber to make the silicone membrane bulge and block the flow path, as shown in Figure 6b, thus interrupting the connection between the PCM storage unit i and the reflow unit.
2. Maintain the heating of valve i while heating the phase change chamber i, causing the paraffin inside to undergo a phase change and generate volume increment, which flows into bellows i connected to PCM storage unit i. As a result, bellows i outputs a linear elongation, driving the gear and shaft to output rotational displacement. At the same time, due to the symmetrical coupling design between the gear and bellows, bellows ii is shortened due to the reverse displacement of the gear, resulting in a decrease in chamber volume. The liquid in bellows ii then flows into the reflow unit through PCM storage unit ii and flow valve ii, as shown in Figure 6c.
3. When it is necessary to stop the joint rotation, stop heating the PCM storage unit i and heat valve i and ii to disconnect the internal liquid from reflow unit for stop the rotation of the joint, as shown in Figure 6d.
4. To output reverse rotational displacement, based on the symmetrical design of this joint, follow steps 1 and 2 to sequentially heat the other side's valve ii and PCM storage unit ii.

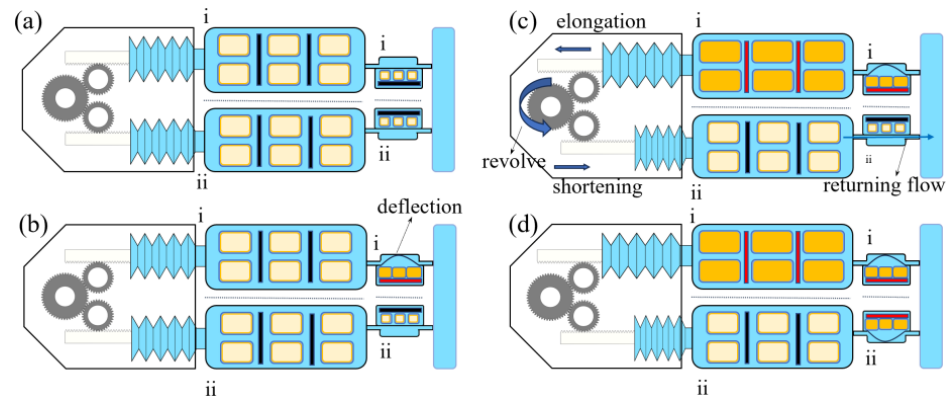


Figure 6. (a) Initial state of the joint; (b) preparatory stage, heating valve unit i; (c) operation stage, heating PCM storage unit i; (d) stop operation.

3. Results

3.1. Driving Experiment with No-Load

3.1.1. Driving Experiment in Air with No Load

This paper conducted numerous laboratory tests on the joint, devising experimental trials with varying heating rates and environmental conditions. The objective was to assess the joint’s response speed and controllability while demonstrating its practical operational capability. The heating methodology and data collection are illustrated in Figure 7a. The details of the equipment used in the experiment are shown in Table 4. Due to the characteristics of the metal ceramics heater (MCH), the resistance of the component continuously changes during the heating process. Hence, it is challenging to precisely control the power through electrical heating. The heating rate was defined based on the heating voltage. When the voltage remains constant, the joint was considered to be in a state of constant heating rate.

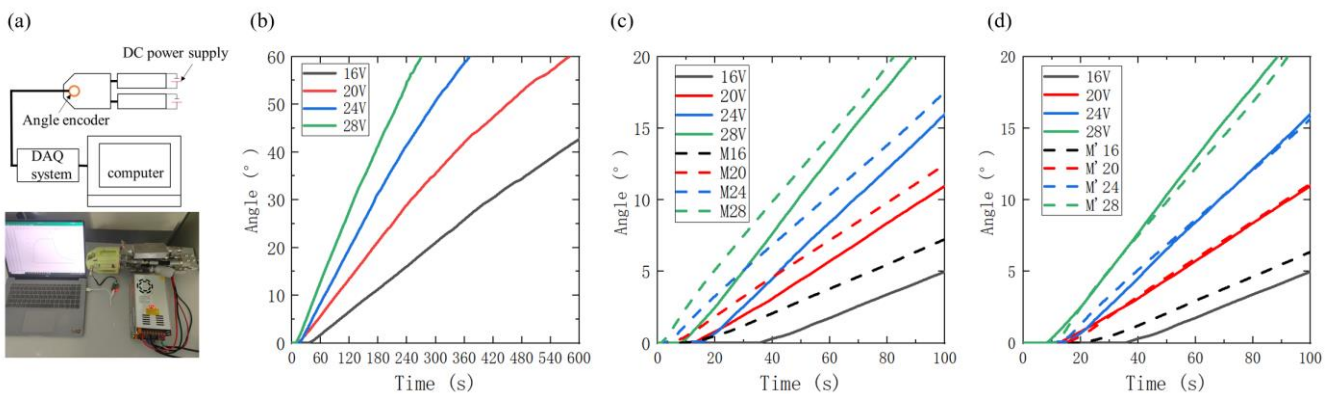


Figure 7. (a) Heating scheme and data acquisition method: direct current power supply provides the necessary energy for phase transition, an angle sensor is connected to the output shaft to record joint displacement data, and a data acquisition system is connected to a computer to store the data, DAQ system: data acquisition system; (b) displacement curves under different heating voltage conditions; (c) simulate the heating of the phase change cavity under the same conditions, and compare the predicted displacement–time curve (dashed line) calculated via the mathematical model with the experimental curve (solid line); (d) comparison of the predicted displacement curve after secondary processing (dashed line) with experimental displacement curve (solid line).

Table 4. Software and hardware models used during the experiments.

Equipment	Model Number
Angular encoder	JY61P
Data acquisition	STM32
Data processing	Matlab

The experiment was divided into four groups, applying different heating voltages of 16 V, 20 V, 24 V, and 28 V to individual PCM storage unit. The maximum heating duration was 600 s, and the maximum rotational angle of the output shaft was 60 degrees. Due to the symmetry of the joint structure, the travel distances for forward and reverse rotations were equal. To simplify the experimental process, both this experiment and subsequent ones involved the unidirectional rotation of the output shaft. The angular displacement of the main shaft was recorded using an angle encoder, as shown in Figure 7b.

From Figure 7b, it can be observed that in the constant heating rate experiments in air, the output shaft speed remained relatively constant. Under the same conditions, the output speed increased with an increase in the heating rate, indicating that the heating rate significantly affected the shaft displacement output. To validate the accuracy of the mathematical model constructed in the previous text, finite element simulations were performed on the phase transition process of the paraffin PCM storage chamber using comsol under the same conditions. Utilizing Equation (6), the predicted displacement curve (the dashed line in Figure 7c of the joint, $X(t)$), was obtained using liquid fraction data at various time points. A comparison between the predicted results (dashed line) and the experimental results (solid line) revealed the following: under identical heating conditions, the joint’s output characteristics predicted by the curve were largely consistent with experimental results. However, the predicted curve exhibited a slight time advancement, indicating that the use of finite element simulation and the mathematical model to predict the driving speed of the phase transition joint aligned well with experimental driving speed. Nevertheless, due to factors such as friction not being taken into account, the predicted joint initiation speed was faster than the experimental result. In order to obtain the better prediction, we use the follow equation to deal with the predicted displacement curve:

$$\begin{cases} X'(t) = X(t - 10) & (t > 10) \\ X'(t) = 0 & (t \leq 10) \end{cases} \quad (7)$$

t represents time, $X(t)$ represents the predicted displacement curve, and $X'(t)$ represents the lagged prediction curve.

Indeed, by introducing a 10 s time lag to the predicted curve, as shown in Figure 7d, it was observed that, except for the case with a heating voltage of 16 V, the predicted curve closely matched the experimental curve. This provides evidence of the basic accuracy of our mathematical model. Consequently, the mathematical model in this study can be used to calculate and predict the phase change driving process under various conditions effectively.

3.1.2. Driving Experiment Underwater with No Load

The main working environment for the joint is underwater. In order to verify the joint’s driving capability underwater, underwater driving experiments with different constant heating voltages were conducted, similar to the experiments described in Section 3.1.1. However, the angle encoder and the DAQ system lack waterproofing capabilities. Overall experimental arrangement is shown in Figure 8a: the PCM storage units and valve units, which require heating and have higher heat exchange rates, are placed underwater, while the transmission unit with less heat dissipation and the DAQ system are placed above water for easy observation and data collection. Due to the thickness of the corrugated tube and the good thermal insulation properties of silicone, the heat dissipation variation caused by the transmission unit placed on the water can be negligibly small.

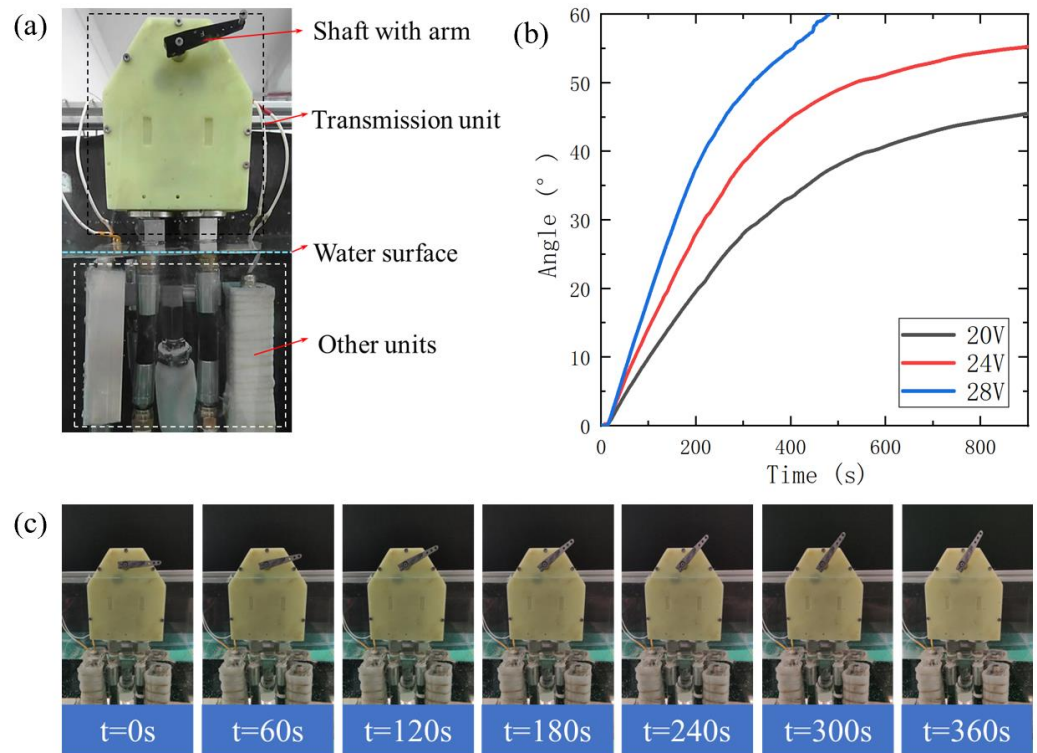


Figure 8. (a) The transmission unit and the output shaft are placed on the water to facilitate data collection, the other units are placed underwater, and the phase change storage unit provides power for underwater heating; (b) displacement curve of different heating voltage valves of driving joints underwater; (c) the screenshots at different moments screenshots of underwater experiment.

The experiment was conducted with three different heating voltages (20 V, 24 V, and 28 V), and the corresponding displacement–time curves are shown in Figure 8b. Unlike the linear output pattern observed in the air Figure 7a, the joint exhibits a fast initial output speed with an approximately linear pattern, and the displacement output path shows smooth variations, with the speed gradually decreasing over time. Overall, the output speed underwater is slower compared to the output speed in the air with the same heating conditions.

The reasons are as follows: in the early stages of the experiment, the internal material undergoes initial melting. During this phase, heat exchange primarily occurs between the liquid paraffin inside the chamber and the solid paraffin. Overall, there is minimal heat dissipation to the environment, resulting in a relatively constant melting rate. As a result, the output characteristics exhibit linearity, similar to what would occur in air. As the phase boundary gradually expands, the heat exchange between the paraffin and the shell increases, leading to an increasing heat dissipation from the shell to the environment. Due to water’s higher heat dissipation rate compared to air, a notable decrease in the speed of underwater convection occurs in the later stages of the phase transition. Additionally, with increasing output displacement and the gradual expansion of the phase boundary, the speed of the phase transition progressively slows down.

3.2. Driving Experiment Underwater with Different Loads

The previous underwater driving experiment confirmed the feasibility of underwater output for this joint. Therefore, in this section, building upon the underwater experiment, the joint was subjected to different loads to further verify its underwater operational capability. To quantify the experimental results and provide a more direct comparison of the joint’s lifting capacity under different loads, the experimental design was similar to the previous section, as shown in Figure 9a. In the initial setup of the experiment, the joint

was positioned at the same initial angle (-20°), and the standard for lifting a weight by rotating it 20° above the horizontal line was established. The joint was supplied with the same heating voltage (28 V), and weights of different loads (0.5 kg, 1 kg, 1.5 kg, 2 kg) were lifted. The displacement–time curves for these scenarios are depicted in Figure 9b.

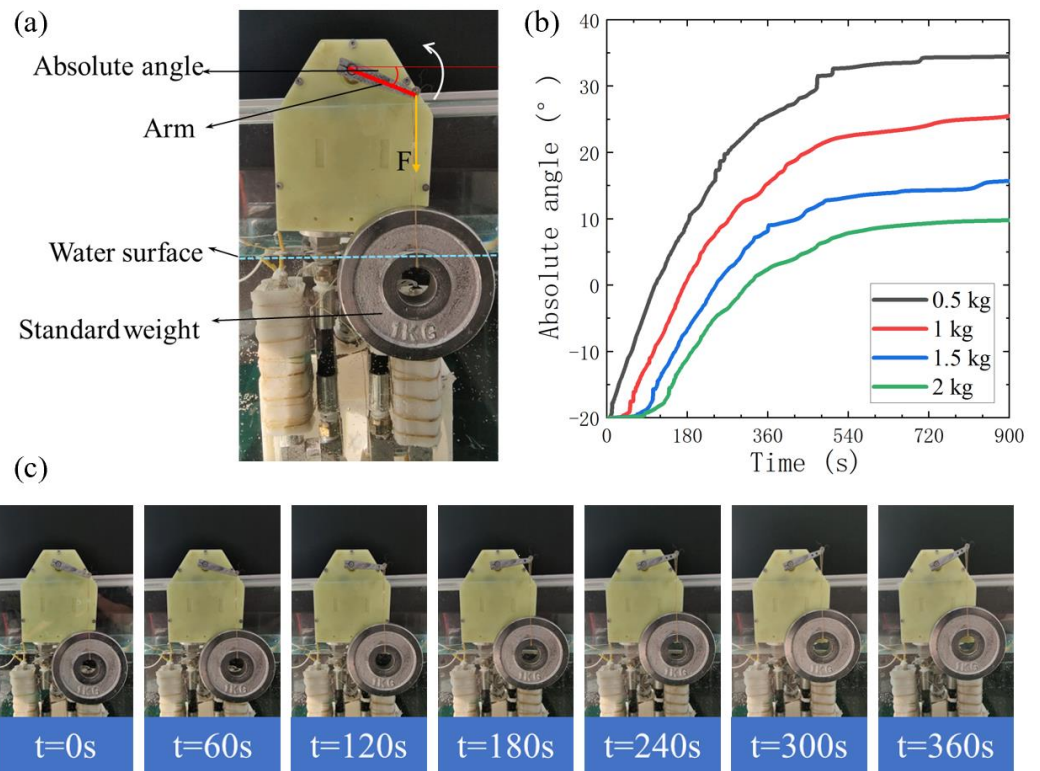


Figure 9. (a) The 4.7 cm servo arm was connected to the spindle, the weights were marked and fixed on the servo arm and the initial angle (-20°) was set, and different weights were lifted by counter-clockwise rotation of the servo arm; (b) the servo arm is driven to lift the displacement–time curves of objects of different masses (0.5 kg/1 kg/1.5 kg/2 kg) with a constant heating voltage; (c) screenshot of the output shaft displacement at different moments of underwater on-load experiment.

Comparing the curves in Figure 8b, it can be observed that the displacement output characteristics of the joint under loaded and unloaded conditions are nearly identical, with the output speed showing a gradual decrease trend. The mass of the load significantly constrains the range of joint displacement output, and as the load increases, the available range of joint displacement gradually diminishes. This reduction is attributed to the increased pressure within the corrugated tube due to the larger load, causing excessive radial expansion, which, in turn, leads to a decrease in axial displacement. As a result, the output capability of the joint declines, and the process is illustrated in Figure 9c.

3.3. Drive Experiment in a Simulative Deep-Sea Environment

In order to validate the feasibility of the joint’s operation in the deep sea, this study conducted simulations of the deep-sea environment based on a high-pressure environment simulation system. As shown in Figure 10a, the joint was horizontally fixed and suspended in the high-pressure environment simulation system. Illumination equipment Figure 10b and camera equipment Figure 10c were used to provide lighting and record the experimental phenomena. The joint’s power cable was connected to a watertight plug above the high-pressure environment simulation system, and the required operating voltage (28 V) was supplied externally. Once the high-pressure environment simulation device was closed and sealed, the internal pressure was raised using the force pump. Initially, the

environment was pressurized to 65 MPa, and the joint was subjected to a constant pressure for 10 min before conducting the joint driving experiments.

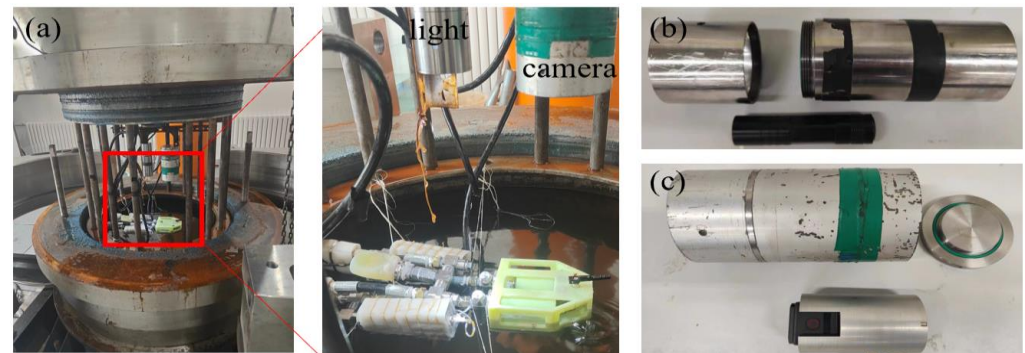


Figure 10. (a) High-pressure environment simulation equipment—fix the joint horizontally so that it is suspended and place light and camera on it; (b) lighting equipment and pressure-resistant housing; (c) camera and pressure-resistant housing.

Real-time screenshots of the experiment are shown in Figure 11. The displacement of the black servo arm at different time points demonstrates that the joint achieved rotational displacement output in the high-pressure environment. The displacement output is nearly consistent with the driving experiments conducted in the underwater environment at atmospheric pressure, confirming the feasibility of the phase-change driving device's operation in deep-sea environments. After the experiment, the device was removed and inspected for any damage. Subsequent driving experiments conducted at atmospheric pressure and high-pressure yielded curves that were essentially identical to the previous measurements, further affirming the reliability and repeatability of the device's operation in high-pressure environments.

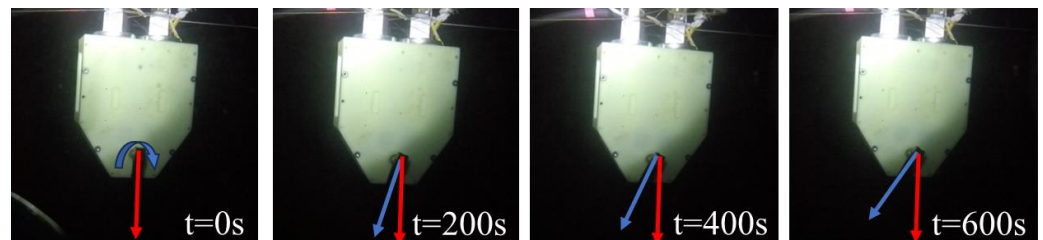


Figure 11. Screenshots of output shaft displacement at different moments in the joint drive experiment at room temperature and high pressure (65 MPa). The red arrow in the figure identifies the position of the output arm of the joint at $t = 0$ s. The blue arrows identify the position of the output arm at different moments of operation.

4. Discussion and Conclusions

This paper introduces a novel, modular, and high-pressure-resistant underwater mechanical joint design. Initially, a solution for a high-pressure-resistant and non-complex pressure-resistant structure flexible actuator was presented. Based on this actuator, a rotary joint mechanism was designed. This design utilizes the symmetrical coupling arrangement of the actuator and the displacement transformation of a gear mechanism to convert unidirectional linear displacement into bidirectional rotary displacement output of the joint. To enhance the joint's operational capabilities, additional units with different functionalities were incorporated into the joint design. This allows the joint to efficiently initiate and halt movements, while also possessing pressure adaptability and the capacity for fluid recirculation.

This study employed an enthalpy-based model to numerically simulate the phase change process of paraffin within a square metal cavity. A mathematical model for the

elongation of a paraffin phase transition-driven device, based on a bellows actuator, was established. The accuracy of the mathematical model was validated in subsequent experiments, demonstrating the predictability of the nonlinear physical process of paraffin phase transition. A series of experimental tests were conducted on the joint to primarily investigate the joint's output characteristics under different environments and varying heating voltages. Drive experiments conducted in air and underwater exhibited two distinct output patterns, i.e., linear and nonlinear, providing theoretical support for future joint control research. Subsequent underwater joint drive experiments with a load indicate that the joint can achieve rotational displacements exceeding 20° under a 2 kg load, demonstrating a certain level of output capability. Lastly, the joint is subjected to drive tests in a high-pressure environment, successfully demonstrating its excellent high-pressure resistance. This experiment suggests the potential for applications in deep-sea environments. As shown in Table 5, we compare various unconventional actuators applied to deep-sea robots. The paraffin actuator used in this joint can operate in a high pressure environment with a relatively low drive voltage, which suggests that this joint has considerable prospects for deep-sea applications.

Table 5. Comparison of actuators in deep-sea machines.

Actuator	Extreme Depth (m)	Robot Scale (cm)	Driving Voltage/Current	Power (W)
paraffin	6500	20	28 V/10 A	205
shape memory alloy [9]	-	3	10 V/60 A	600
dielectric elastomer [10]	10,900	-	8000 V/-	-
piezoelectric [11]	2000	5	300 V/-	-

In the future, we plan to downsize the overall dimensions of the joint. As the majority of the components in this joint are standard parts, ensuring compactness in the structure is challenging. Therefore, we intend to pursue non-standard designs for the joint to identify the optimal geometric parameters. In the experiments conducted in this study, the joint's driving speed was relatively slow, mainly due to the limitation of the melting speed of paraffin. We plan to delve into the methods to enhance paraffin's heat transfer capabilities based on materials like nano-graphite, the exploration of paraffin unit shapes, and the design of heating strategies. In load experiments, it is noticeable that the joint's output capacity is relatively low, and the output characteristics exhibited nonlinearity. Consequently, we further optimize the joint's sealing and output transmission structure to attain improved output capacity and characteristics.

Author Contributions: D.N. initiated and supervised all the research. D.N., X.H. and J.H. conducted and orchestrated the majority of experimental tasks and conducted the analysis of resulting data. G.L. assisted in the writing of the manuscript. G.L. and K.Z. contributed to the development and verification of research concepts. All authors discussed the results and contributed to the writing of the manuscript. All authors have read and agreed to the published version of the manuscript.

Funding: This work was supported by the Fundamental Research Funds for the Central Universities (3132023513, 3132023124), the National Nature Science Foundation of China (52075064, 51405054), Dalian Innovation Program (2018RQ19), and Open Foundation of the State Key Laboratory of Fluid Power and Mechatronic Systems (GZKF-201810).

Institutional Review Board Statement: Not applicable.

Informed Consent Statement: Not applicable.

Data Availability Statement: Data are contained within the article.

Acknowledgments: Authors want to thank technicians operating test equipment for supporting this study.

Conflicts of Interest: The authors declare no conflict of interest.

References

1. Danovaro, R.; Fanelli, E.; Aguzzi, J.; Billett, D.; Carugati, L.; Corinaldesi, C.; Dell Anno, A.; Gjerde, K.; Jamieson, A.J.; Kark, S. Ecological variables for developing a global deep-ocean monitoring and conservation strategy. *Nat. Ecol. Evol.* **2020**, *4*, 181–192. [[CrossRef](#)] [[PubMed](#)]
2. Proud, R.; Cox, M.J.; Brierley, A.S. Biogeography of the global ocean's mesopelagic zone. *Curr. Biol.* **2017**, *27*, 113–119. [[CrossRef](#)] [[PubMed](#)]
3. Reygondeau, G.; Guidi, L.; Beaugrand, G.; Henson, S.A.; Koubbi, P.; MacKenzie, B.R.; Sutton, T.T.; Fioroni, M.; Maury, O. Global biogeochemical provinces of the mesopelagic zone. *J. Biogeogr.* **2018**, *45*, 500–514. [[CrossRef](#)]
4. Li, J.; Wang, P. Discovery of deep-water bamboo coral forest in the South China Sea. *Sci. Rep.* **2019**, *9*, 15453. [[CrossRef](#)] [[PubMed](#)]
5. Yang, B.; Liu, Y.; Liao, J. Manned Submersibles—Deep-sea Scientific Research and Exploitation of Marine Resources. *Bull. Chin. Acad. Sci. (Chin. Version)* **2021**, *36*, 622–631.
6. Hildebrandt, M.; Kerdels, J.; Albiez, J.; Kirchner, F. A Multi-Layered Controller Approach for High Precision End-Effector Control of Hydraulic Underwater Manipulator Systems. In Proceedings of the OCEANS 2009, Biloxi, MS, USA, 26–29 October 2009; pp. 1–5.
7. Li, L.; Wu, J. Deformation and leakage mechanisms at hydraulic clearance fit in deep-sea extreme environment. *Phys. Fluids* **2020**, *32*, 067115. [[CrossRef](#)]
8. Tian, Q.; Zhang, Q.; Chen, Y.; Huo, L.; Li, S.; Wang, C.; Bai, Y.; Du, L. Influence of Ambient Pressure on Performance of a Deep-Sea Hydraulic Manipulator. In Proceedings of the OCEANS 2019, Marseille, France, 17–20 June 2019; pp. 1–6.
9. Singh Matharu, P.; Wang, Z.; Costello, J.H.; Colin, S.P.; Baughman, R.H.; Tadesse, Y.T. SoJel—A 3D printed jellyfish-like robot using soft materials for underwater applications. *Ocean Eng.* **2023**, *279*, 114427. [[CrossRef](#)]
10. Li, G.; Chen, X.; Zhou, F.; Liang, Y.; Xiao, Y.; Cao, X.; Zhang, Z.; Zhang, M.; Wu, B.; Yin, S. Self-powered soft robot in the Mariana Trench. *Nature* **2021**, *591*, 66–71. [[CrossRef](#)] [[PubMed](#)]
11. Li, K.; Zhou, X.; Liu, Y.; Sun, J.; Tian, X.; Zheng, H.; Zhang, L.; Deng, J.; Liu, J.; Chen, W. A 5 cm-Scale Piezoelectric Jetting Agile Underwater Robot. *Adv. Intell. Syst.* **2023**, *5*, 2200262. [[CrossRef](#)]
12. Bu, K.; Gong, X.; Yu, C.; Xie, F. Biomimetic Aquatic Robots Based on Fluid-Driven Actuators: A Review. *J. Mar. Sci. Eng.* **2022**, *10*, 735. [[CrossRef](#)]
13. Wilhelm, E.; Richter, C.; Rapp, B.E. Phase change materials in microactuators: Basics, applications and perspectives. *Sens. Actuators A Phys.* **2018**, *271*, 303–347. [[CrossRef](#)]
14. Ogden, S.; Klintberg, L.; Thornell, G.; Hjort, K.; Bodén, R. Review on miniaturized paraffin phase change actuators, valves, and pumps. *Microfluid. Nanofluid.* **2014**, *17*, 53–71. [[CrossRef](#)]
15. Lyu, F.; Li, M.; Guo, J.; Guo, S. A New Fabrication Method for Soft Pneumatic Actuators based on Paraffin. In Proceedings of the 2022 IEEE International Conference on Mechatronics and Automation (ICMA), Guilin, China, 7–10 August 2022; pp. 340–344.
16. Svensson, S.; Sharma, G.; Ogden, S.; Hjort, K.; Klintberg, L. High-pressure peristaltic membrane micropump with temperature control. *J. Microelectromech. Syst.* **2010**, *19*, 1462–1469. [[CrossRef](#)]
17. Liu, B.; Yang, J.; Yang, J.; Li, D.; Gao, G.; Wang, Y. A thermally actuated microvalve using paraffin composite by induction heating. A thermally actuated microvalve using paraffin composite by induction heating. *Microsyst. Technol.* **2019**, *25*, 3969–3975. [[CrossRef](#)]
18. Hou, J.; Zou, W.; Li, Z.; Gong, Y.; Burnashev, V.; Ning, D. Development and experiments of an electrothermal driven deep-sea buoyancy control module. *Micromachines* **2020**, *11*, 1017. [[CrossRef](#)] [[PubMed](#)]
19. Ning, D.; Li, Z.; Liang, G.; Wang, Q.; Zou, W.; Gong, Y.; Hou, J. Design and Performance Study for Electrothermally Deep-Sea Drive Microunits Using a Paraffin Phase Change Material. *Micromachines* **2021**, *12*, 415. [[CrossRef](#)] [[PubMed](#)]
20. Wołoszyn, J.; Szopa, K.; Czerwiński, G. Enhanced heat transfer in a PCM shell-and-tube thermal energy storage system. *Appl. Therm. Eng.* **2021**, *196*, 117332. [[CrossRef](#)]

Disclaimer/Publisher's Note: The statements, opinions and data contained in all publications are solely those of the individual author(s) and contributor(s) and not of MDPI and/or the editor(s). MDPI and/or the editor(s) disclaim responsibility for any injury to people or property resulting from any ideas, methods, instructions or products referred to in the content.